crystals

MDPI

Article

Aero-TiO_2 Prepared on the Basis of Networks of ZnO Tetrapods

Vladimir Ciobanu [1,*], Veaceslav V. Ursaki [1,2], Sebastian Lehmann [3], Tudor Braniste [1], Simion Raevschi [4], Victor V. Zalamai [1], Eduard V. Monaico [1], Pascal Colpo [5], Kornelius Nielsch [3] and Ion M. Tiginyanu [1,2]

1 National Center for Materials Study and Testing, Technical University of Moldova, 2004 Chisinau, Moldova
2 Academy of Sciences of Moldova, 2001 Chisinau, Moldova
3 Institute for Metallic Materials (IMW), Leibniz Institute of Solid State and Materials Research (IFW Dresden), Helmholtzstrasse 20, 01069 Dresden, Germany
4 Department of Physics and Engineering, State University of Moldova, Alexei Mateevici Str. 60, 2009 Chisinau, Moldova
5 European Commission, Joint Research Centre, 21027 Ispra, Italy
* Correspondence: vladimir.ciobanu@cnstm.utm.md

Abstract: In this paper, new aeromaterials are proposed on the basis of titania thin films deposited using atomic layer deposition (ALD) on a sacrificial network of ZnO microtetrapods. The technology consists of two technological steps applied after ALD, namely, thermal treatment at different temperatures and etching of the sacrificial template. Two procedures are applied for etching, one of which is wet etching in a citric acid aqua solution, while the other one is etching in a hydride vapor phase epitaxy (HVPE) system with HCl and hydrogen chemicals. The morphology, composition, and crystal structure of the produced aeromaterials are investigated depending on the temperature of annealing and the sequence of the technological steps. The performed photoluminescence analysis suggests that the developed aeromaterials are potential candidates for photocatalytic applications.

Keywords: aero-TiO_2; atomic layer deposition; titania; anatase; rutile; spinel; zinc titanate; sacrificial template; annealing; luminescence

Citation: Ciobanu, V.; Ursaki, V.V.; Lehmann, S.; Braniste, T.; Raevschi, S.; Zalamai, V.V.; Monaico, E.V.; Colpo, P.; Nielsch, K.; Tiginyanu, I.M. Aero-TiO_2 Prepared on the Basis of Networks of ZnO Tetrapods. *Crystals* **2022**, *12*, 1753. https://doi.org/10.3390/cryst12121753

Academic Editor: Giuseppe Prestopino

Received: 9 November 2022
Accepted: 1 December 2022
Published: 3 December 2022

1. Introduction

A series of extra highly porous and ultra-lightweight aeromaterials has emerged as a new class of nanomaterials for electronic, photonic, energy conversion and storage, sensor, catalysis, and biomedical applications [1–4]. Graphene aerogels (GAs) [5] and Aerographite (AG) [6] have been demonstrated to be promising scaffolds for the deposition of various solid-state nanoparticles, resulting in the formation of hybrid nanocomposite materials with flexible three-dimensional (3D) architectures, such as ZnO-AG [7], GaN-AG [8], CdS-GA [9], and InP-AG [10] nanocomposites.

Most of these AG materials are prepared on the basis of highly porous ZnO networks of interconnected micrometer-thick rods with a 3D architecture, often in the shape of tetrapods. These networks are prepared by using simple and cost-effective flame transport technology, and they serve as sacrificial templates [11]. AG networks are produced using a one-step chemical vapor deposition (CVD) process with toluene to transform ZnO tetrapods into graphite cylinders [12].

In hydride vapor-phase epitaxy (HVPE) processes with Ga and N [13] or Cd and S precursors [14], aero-GaN or aero-ZnS is produced, respectively. In the first process, GaN deposition is combined with ZnO template removal, which enables one to fabricate GaN hollow interconnected microtetrapods with a wall thickness in the nanometer scale, while in the second process, CdS is deposited on the sacrificial template with simultaneous or subsequent transformation of CdS into ZnS and the removal of the sacrificial ZnO template.

Both aero-GaN and aero-ZnS materials have been proven to be hydrophilic under tension and hydrophobic when compressed against water, making them promising for applications in microfluidic devices, microrobotics, and sensorics. In particular, due to the

photocatalytic properties of these materials, fluorescent micromotors have been demonstrated in the presence of a hydrogen peroxide solution, and self-propelled liquid marbles have been developed [14,15]. Apart from that, aero-GaN is an electromagnetic interference (EMI) shielding material with good performances in the X-band [16] and THz frequencies [17], and it is suitable for the fabrication of robust pressure sensors [18].

Aero-Ga_2O_3 is another aero-nanomaterial, and it was produced as a result of aero-GaN oxidation [19,20]. It exhibits photocatalytic activity as well as extremely low reflectivity and high transmissivity in an ultrabroadband electromagnetic spectrum ranging from the X-band (8–12 GHz) to several terahertz, which opens possibilities for new applications [19,20].

In this context, the development of TiO_2 aero-nanomaterials, called aero-TiO_2 or *Aerotitania*, is expected to be a prospective direction of investigations. Titania exists in several crystallographic modifications, of which anatase and rutile polymorphs are most stable under ambient conditions. Both phases can be photoactivated by UV light, the anatase phase being found to exhibit higher photocatalytic activity than the rutile phase. Note that titania nanoparticles have been used in a wide range of applications, such as photocatalysts [21–24], dye-sensitized solar cells [25], gas sensors [26], and nanomedicine [27], due to their nontoxicity, cost effectiveness, and high stability. It has been shown that immobilizing anatase nanoparticles on ZnO tetrapods using the vapor hydrolysis method significantly enhances the photooxidation reaction of phenol [28].

Apart from anatase and rutile phases, a ternary Zn_2TiO_4 phase is often formed when ZnO and TiO_2 are mixed in technological processes. This phase is also photocatalytic-active [29–33], and it can be used in propanol [34] and acetone [35] gas sensing. ZnO/Zn_2TiO_4 core/shell nanowires have been proposed for the photocatalytic oxidation of acetone [36]. Rh-doped Zn_2TiO_4 photocatalysts and Zn_2TiO_4 nanowires have been used for hydrogen generation from water [37,38].

Rare-earth elements can efficiently be doped in the Zn_2TiO_4 matrix up to the solubility limit of approximately 0.5 at% [39], which makes the material highly luminescent and suitable for implementation in facile microfluidic devices to detect and remove heavy-metal ions [40] and in white light-emitting diodes (WLEDs) for display applications [41].

A suitable deposition technique should be used for the preparation of TiO_2 aero-materials on the basis of networks of interconnected ZnO microtetrapods. Atomic layer deposition (ALD) is an extremely valuable technique for growing conformal ultrathin films with high accuracy on different substrates [42]. It has been shown that ALD coatings provide a high stability to various functional nanostructures, improving their performance for applications in photovoltaics, electrochemical energy storage, photo- and electro-chemical devices, etc. [43]. In particular, it has been found that conformal ALD TiO_2 coatings on ZnO nanoparticles significantly improve the photostability of the material, concomitantly maintaining its high photocatalytic activity [44]. ALD has also been applied for the preparation of TiO_2/ZnO double-layer hollow fibers through a consecutive deposition of TiO_2 and ZnO layers on sacrificial polymer fibers, followed by thermal treatment, and it has been shown that the prepared material is highly sensitive to reducing gases [45].

The goal of this paper is to develop technologies for the preparation of TiO_2-related aeromaterials with controlled phase composition on the basis of networks of interconnected ZnO microtetrapods coated with TiO_2 thin films using ALD, taking into account the previous exploration of composites in the TiO_2–ZnO system for various practical applications.

2. Materials and Methods

A sacrificial network of ZnO microtetrapods was prepared using a simple flame transport approach, which is described elsewhere [11]. The produced powder was pressed in an inox chamber with dimensions of 24 × 12 mm^2 to prepare tablet samples with a 2 mm thickness. In order to increase the mechanical stability, the tablets, with a density of 0.5 g/cm^3, were annealed at 1100 °C for 1 h in air.

TiO_2 films were deposited using a thermal ALD reactor, Veeco Savannah S200 from Veeco Instruments Inc. (Plainview, New York, NY, USA), equipped with a disk-like chamber

(diameter = 300 mm, height = 7 mm). $TiCl_4$ was used as the Ti precursor, and deionized water (H_2O) was used as the oxygen source. The reaction temperature for TiO_2 deposition was set to 150 °C. High-purity N_2 was used as the carrier gas, and the chamber was kept at a flow rate of 20 sccm during the ALD reaction process. The optimized pulse and purge times were 0.2/120/0.015/120 s for one ALD deposition cycle of TiO_2 ($TiCl_4/N_2/H_2O/N_2$). It was found that a 200 ms pulse time for $TiCl_4$ is enough to saturate the surface [46]. Due to the low reactivity of $TiCl_4$ with H_2O, an exposure time of 60 s with closed valves was added to fully allow the precursors to react.

With respect to the large surface areas of the samples, the exposure times were kept low, and the purge times were kept high to ensure the self-limiting character of the ALD process. The growth rate of TiO_2 was determined to be around 0.16 nm/cycle by measuring the thickness of Si wafers using a spectroscopic ellipsometer (SENpro, SENTECH Instruments GmbH, Berlin, Germany), as reported elsewhere [47,48]. In total, 310 cycles were applied for the TiO_2 coatings. The ellipsometry measurements of the Si wafers next to the sample used as a reference showed an actual thickness of 46 nm.

The etching of the sacrificial ZnO template was performed either in a citric acid aqua solution of 0.1 M at room temperature (wet etching) for 72 h or in a hydride vapor-phase epitaxy (HVPE) system with hydrogen chloride (HCl) gas and hydrogen (H_2) used as reaction materials and carrier gases at a temperature of 800 °C. The thermal treatment of the samples was performed either before or after the etching in the citric acid solution at 400 °C or 800 °C in air for 1 h.

The morphology of the prepared samples was studied using an FEI-Nova NanoLab 600i DualBeam (FEI Company, Hillsboro, OR, USA) scanning electron microscope (SEM), equipped with EDX detector-analyzer Ametek model ELECT PLUS for a chemical analysis of the samples. An X-ray diffraction analysis was performed with a Bruker AXS D8 DISCOVER X-ray diffractometer (XRD, Bruker Italia S.r.l., Milano, Italy) in a standard θ–2θ Bragg–Brentano configuration, with Cu Kα1 radiation (λ = 0.15406 nm) operating at a 40 kV beam voltage and a 40 mA beam current. Diffraction data were collected in the range of 20–80° with a step length of 0.025°.

Raman scattering (RS) spectra were recorded at room temperature with a Renishaw inVia Qontor confocal microscope (Renishaw plc, Wotton-under-Edge, UK) equipped with a laser excitation source of 532 nm (50 mW). A (100×) microscope objective lens was selected to focus the light on the sample surface. System calibration was performed on a monocrystalline Si wafer with a main peak measured at 521 cm^{-1}. A total of 10 spectra were collected, with a 10 s exposure time and 5% laser power for each measurement.

The photoluminescence (PL) was excited by a 325 nm He-Cd laser (Kimmon, Tokyo, Japan), with the samples mounted on the cold station of an LTS-22-C-330 (US Cryogenics INC., Vancouver, WA, USA) optical cryogenic system. The emission was analyzed in a quasi-backscattering geometry through a double SDL-1 spectrometer (LOMO, Sankt Petersburg, USSR). The signal of an FEU-106 photomultiplier (MELZ, Moscow, Russia) with an SbKNaCs photocathode working in a photon counting mode was introduced using an IBM computer.

3. Results and Discussion

The initial ZnO template consisting of microtetrapods with cylindrical microrod arms (Figure S1) was transformed into cylindrical TiO_2 microtubes after etching the sample in a citric acid solution and annealing at 400 °C, as illustrated in Figure 1a. In some cases, a thin ZnO layer was found on the inner surface of the microtubes. The cylindrical film proved to be quite dense and solid. A structure with a similar morphology was produced upon etching the sample in a citric acid solution and annealing at 800 °C (Figure 1b). The structure produced by etching the initial template in the HVPE system consisted of perforated microtubes, as shown in Figure 1c.

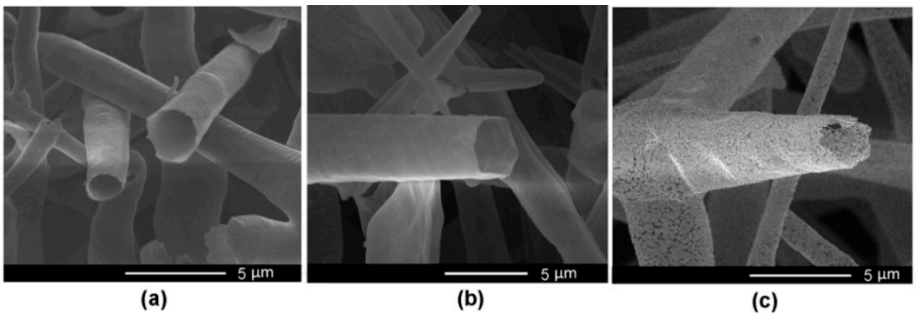

Figure 1. (**a**) SEM image of a sample etched in citric acid and annealed at 400 °C; (**b**) a sample etched in citric acid and annealed at 800 °C; (**c**) a sample etched in the HVPE system at 800 °C.

The EDX analysis of the initial sample showed that it formed from ZnO microrods covered by a thin TiO_2 layer (Figure S2). The EDX analysis of the sample annealed at 400 °C with subsequent etching in the citric acid (Figure 2a) suggests that it consisted of a TiO_2 phase and a thin ZnO film remaining on the inner surface of the TiO_2 microtubes after etching. Similar results were obtained for a sample prepared by etching in the HVPE system (Figure S3). However, some trace of chlorine from the HVPE process was found in the sample. However, the sample annealed at 800 °C with subsequent etching in citric acid showed a nearly stoichiometric Zn_2TiO_4 composition within the limits of errors of the EDX system, which are around 1 at% for Zn and Ti and around 5 at% for O (Figure 2b).

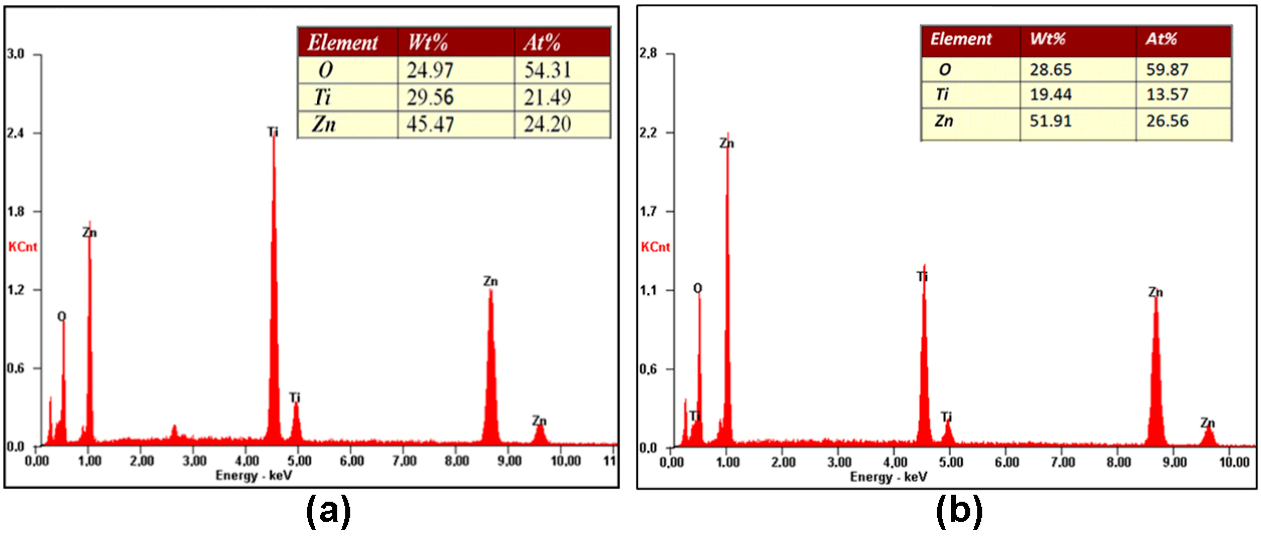

Figure 2. (**a**) Results of EDX analysis of a sample annealed at 400 °C with subsequent etching in citric acid and (**b**) a sample annealed at 800 °C with subsequent etching in citric acid.

The XRD analysis of the as-grown sample (Figure 3a, curve 1) shows reflexes corresponding to the wurtzite ZnO phase according to the PDF code no. 00-036-1451 [49] and JCPDS card no. 00-005-0664 [50], which demonstrates the high crystalline quality of the ZnO template.

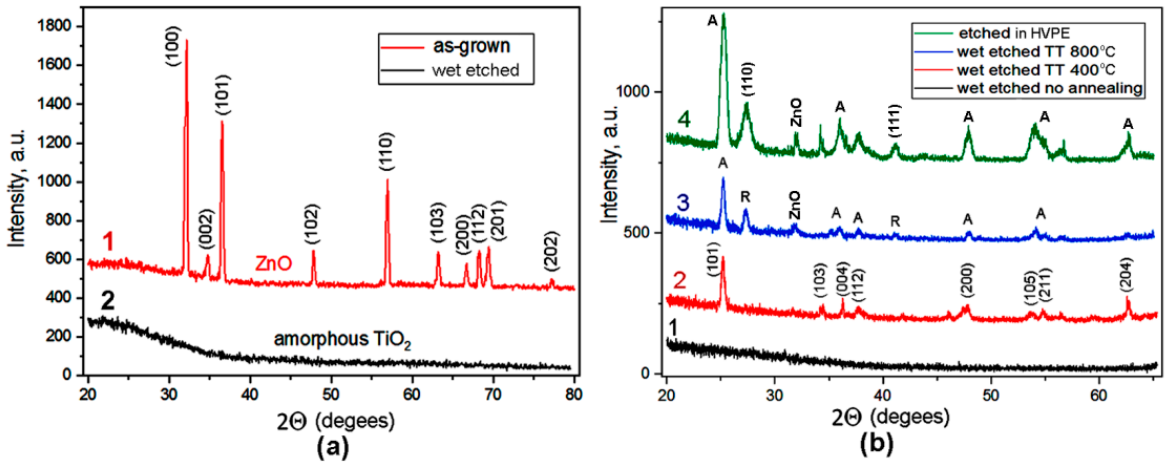

Figure 3. (**a**) XRD pattern of the as-grown sample before (curve 1) and after (curve 2) wet etching. (**b**) XRD pattern of samples subjected to wet etching without annealing (curve 1) and with annealing at 400 °C (curve 2) and 800 °C (curve 3), as well as a sample etched in the HVPE system (curve 4). The reflexes on curve 2 are indicated for the anatase phase, while those on curve 4 are indicated for the rutile phase.

The XRD patterns of samples etched in the citric acid solution with subsequent thermal treatment (TT) at different temperatures, as well as of a sample etched in the HVPE system, are shown in Figure 3b. Again, the wet-etched sample without annealing is amorphous (curve 1). The wet-etched sample annealed at 400 °C exhibits reflexes from the TiO_2 anatase phase according to JCPDS no. 00-004-0477 [22,23,50], while both samples prepared using wet etching with subsequent annealing at 800 °C and that prepared using etching in the HVPE system contain reflexes from the rutile phase (JCPDS no. 00-004-0551) [22,23,50], in addition to reflexes from the anatase phase. Therefore, one can conclude that the sample prepared using wet etching with subsequent annealing at 400 °C only contains the anatase phase, while the other samples represent a mixture of anatase and rutile phases.

The reversal of the etching and annealing steps does not significantly change the composition of the obtained sample when annealing is performed at 400 °C. In both cases, the produced samples have an anatase TiO_2 phase. However, the XRD analysis suggests that the crystalline quality of the sample firstly etched and then annealed (curve 2 in Figure 3b) is better than the quality of the sample firstly annealed and then etched (curve 2 in Figure 4a). The situation is different for samples annealed at 800 °C. While the sample firstly etched and then annealed (curve 3 in Figure 3b) represents a mixture of anatase and rutile phases, the sample firstly annealed and then etched (curve 2 in Figure 4b) is of a pure Zn_2TiO_4 phase indexed according to the JCPDS card no. 00-019-1483 [50]. The reflexes marked with asterisk in Figure 4b (curve 1) refer to the Zn_2TiO_4 phase, but they are slightly shifted with respect to those of curve 2.

The XRD data are corroborated by the Raman scattering analysis. The sample with the sacrificial template removed via wet etching without thermal treatment discloses the amorphous nature of the TiO_2 coating, with no Raman peaks observed in the spectrum (curve 1 in Figure 5a). The Raman spectrum of a sample wet-etched with subsequent annealing at 400 °C exhibits peaks from the anatase phase (curve 2 in Figure 5a). The anatase TiO_2 (space group D_{4h}^{19} – $I4_1/amd$) has six Raman-active vibrations: $A_{1g} + 2B_{1g} + 3E_g$ [51]. Four of these modes situated at 143 cm^{-1}, 397 cm^{-1}, 517 cm^{-1}, and 639 cm^{-1} prevail in the Raman spectrum, being attributed to $E_g(1)$, $B_{1g}(1)$, a superposition of $B_{1g}(2)$ and A_{1g}, and $E_g(3)$, respectively. A weak peak is also observed at 197 cm^{-1}, corresponding to the $E_g(2)$ vibration.

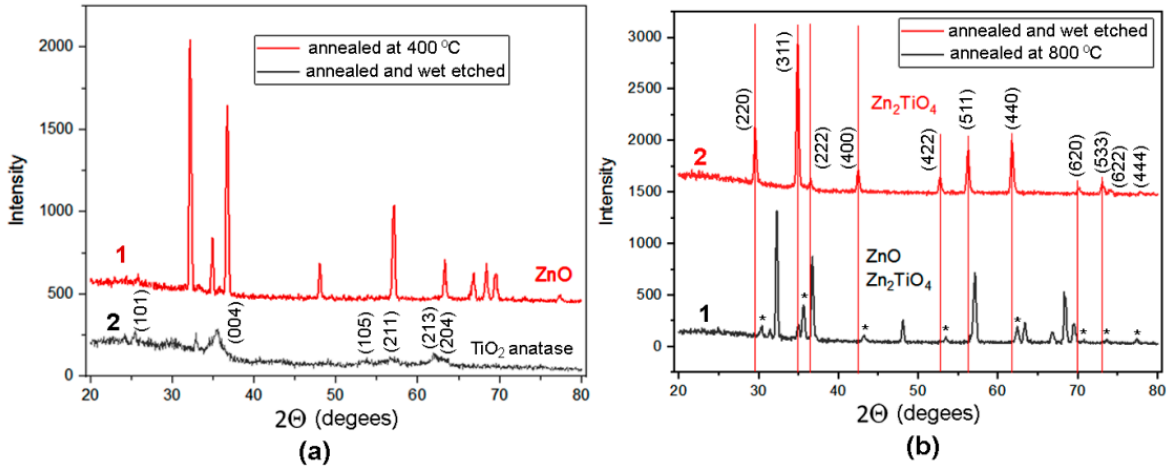

Figure 4. (**a**) XRD pattern of a sample annealed at 400 °C without etching (curve 1) and a sample subjected to wet etching after annealing at 400 °C (curve 2). (**b**) XRD pattern of a sample annealed at 800 °C without etching (curve 1) and a sample subjected to wet etching after annealing at 800 °C (curve 2).

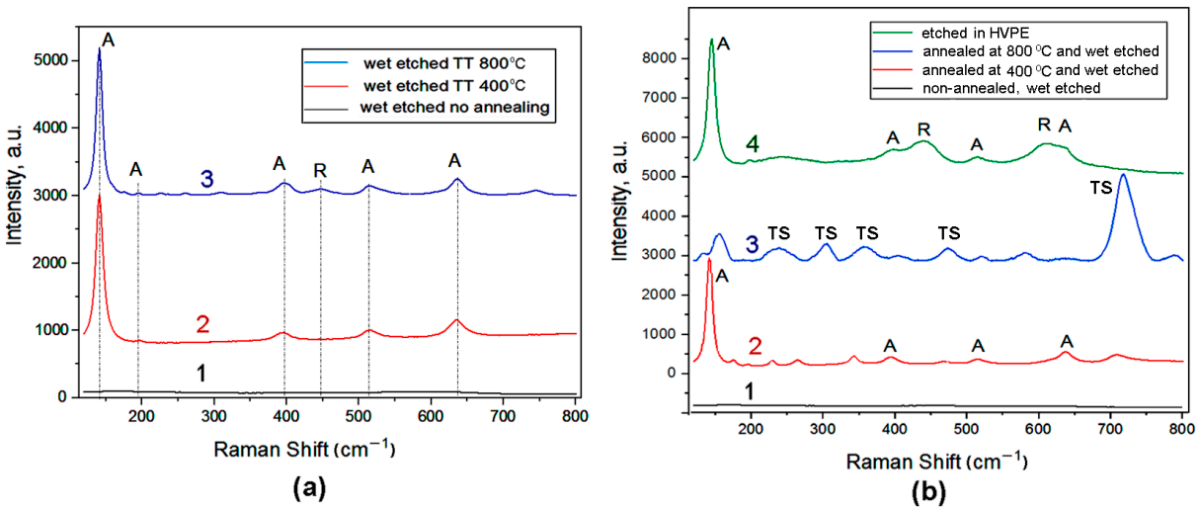

Figure 5. (**a**) Raman spectra of a sample subjected to wet etching without annealing (curve 1) and with annealing at 400 °C (curve 2) and 800 °C (curve 3). (**b**) Raman spectra of a non-annealed wet-etched sample (curve 1), a sample annealed at 400 °C with subsequent wet etching (curve 2), a sample annealed at 800 °C with subsequent wet etching (curve 3), and a sample etched in the HVPE system at 800 °C (curve 4). The notations A, R, and TS mean anatase, rutile, and ternary spinel Zn_2TiO_4, respectively.

An additional weak band is observed at 447 cm^{-1} in the spectrum of the sample wet-etched with subsequent annealing at 800 °C (curve 3 in Figure 5a), which comes from the rutile phase, suggesting that this sample represents a mixture of anatase and rutile phases, as also demonstrated by the XRD analysis. The rutile structure of titania belongs to the space group D^{14}_{4h}, and it has four Raman-active vibrations: $A_{1g} + B_{1g} + B_{2g} + E_g$ [52,53]. The band at 447 cm^{-1} corresponds to the E_g mode.

The Raman spectrum from the sample annealed at 400 °C with subsequent wet etching (curve 2 in Figure 5b), similarly to the sample etched and annealed, i.e., with reversed technological steps, is also dominated by the peaks coming from the anatase vibrational modes, while the spectrum of the sample annealed in the HVPE system (curve 4 in Figure 5b) represents a combination of vibrational modes related to both anatase and rutile phases, similarly to the XRD data presented by curve 4 in Figure 3b. Apart from

the four vibrational modes related to the anatase phase and marked as A in Figure 5b, the spectrum of the sample annealed in the HVPE system reveals two modes at 447 cm^{-1} and 612 cm^{-1} assigned to E_g and A_{1g} of the rutile phase, respectively. A band with the maximum around 250 cm^{-1} is also observed in the spectrum, which is usually assigned to second-order Raman scattering in the rutile phase [53].

Regarding the sample annealed at 800 °C with subsequent wet etching, the Raman scattering analysis confirms the results of the XRD analysis indicating that it consists of a ternary spinel-type Zn_2TiO_4 compound. This compound belongs to the Fd-3m space group with 56 atoms in the unit cell, in which 32 oxygen atoms comprise a face-centered cubic lattice with associated interstitial octahedral (O) and tetrahedral (T) sites. The T sites are occupied by half of the divalent Zn cations, while the O sites are randomly filled with a stoichiometric mixture of divalent Zn and tetravalent Ti cations. Nevertheless, the smallest Bravais cell contains only 14 atoms, and, according to the factor group analysis, the irreducible representations of the vibration modes at the Γ point are described as $A_{1g}(R)$ + $E_g(R)$ + F_{1g}+ $3F_{2g}(R)$ + $2A_{2u}$ + $2E_u$ + $4F1_u(IR)$ + $2F_{2u}$, of which five modes are Raman-active, including $A_{1g}(R)$, $E_g(R)$, and $3F_{2g}(R)$ [54]. The Raman spectrum of the sample is dominated by the A_{1g} mode at 720 cm^{-1}. The peak at 475 cm^{-1} is indexed as the E_g mode, while the peaks at 250 cm^{-1}, 308 cm^{-1}, and 350 cm^{-1} are attributed to the F_{2g} modes [54]. The peaks at 154 cm^{-1}, 570 cm^{-1}, and 794 cm^{-1} are also observed in the spectrum. It has previously been suggested that these vibrations do not belong to the first-order Raman modes of Zn_2TiO_4 [54].

Luminescence was investigated to assess the presence of defects in the prepared samples. Figure 6 compares the PL spectra of samples annealed at 400 °C (Figure 6a) and 800 °C (Figure 6b) with subsequent etching in citric acid solutions. The PL spectra cover a wide energy range from 2.0 eV to 3.5 eV in both samples. They consist of a high-energy PL band with the maximum around 3.0 eV and a low-energy band with the maximum around 2.5 eV, with the intensity of the low-energy band being higher in the sample annealed at 800 °C. Apart from that, one can see that the intensity of the high-energy band is quenched stronger than the intensity of the low-energy band with an increase in the temperature from 10 K to room temperature. The PL spectra of the sample prepared via etching in the HVPE system are similar to those of the samples annealed at 400 °C with subsequent etching in citric acid solutions. However, the high-energy emission band is slightly shifted to lower photon energy (Figure S4).

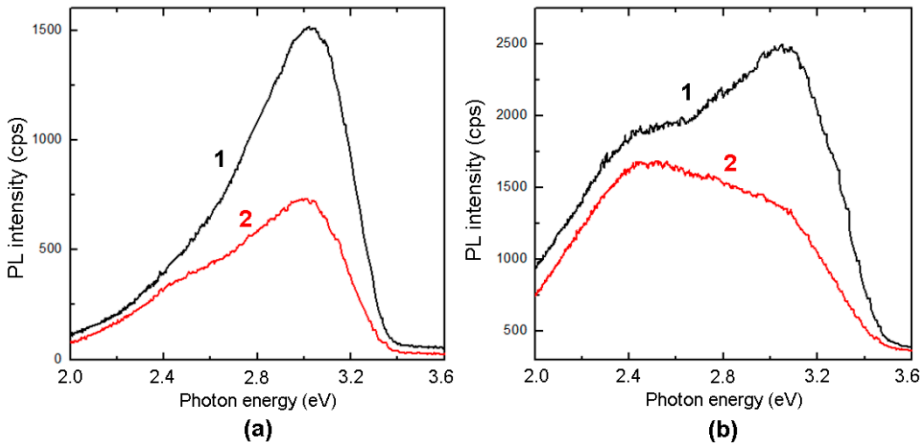

Figure 6. (**a**) PL spectra of samples annealed at 400 °C and (**b**) 800 °C with subsequent etching in citric acid solutions, measured at 10 K (curve 1) and at room temperature (curve 2).

The deconvolution of the PL spectra shown in Figure 7 indicates that the spectra consist of three energy bands, namely, one green band and two violet bands. The green band is situated at 2.5–2.6 eV, and the first violet band is situated at 2.9–3.0 eV. The second violet band is centered at 3.1 eV and 3.2 eV in the samples annealed at 400 °C and 800 °C,

respectively. The deconvolution of the PL spectra of the sample prepared via etching in the HVPE system showed that the high-energy PL band is shifted by around 0.1 eV to lower photon energy, with it being centered at 3.03 eV (Figure S5).

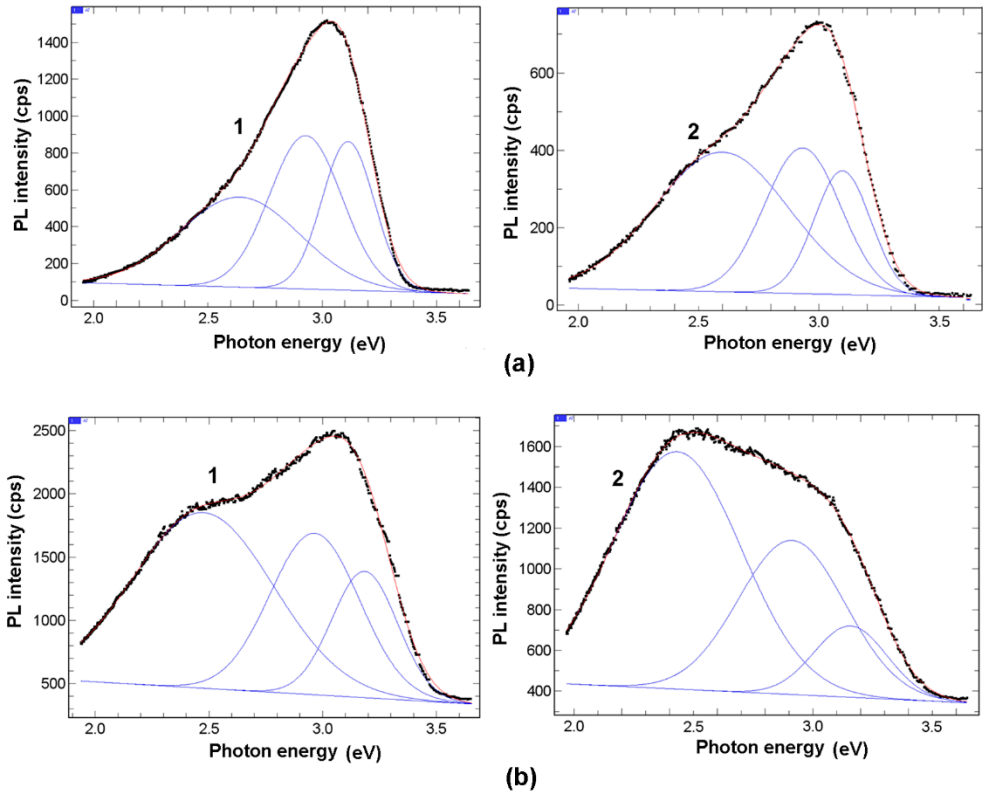

Figure 7. Deconvolution of PL spectra for samples annealed at (**a**) 400 °C and (**b**) 800 °C, with subsequent etching in citric acid solution. The spectra were measured at 10 K (curve 1) and at room temperature (curve 2).

As demonstrated by the XRD analysis, the sample annealed at 400 °C is formed from TiO_2 microtubes with an anatase structure. As shown in previous investigations, the bandgap of the anatase phase is 3.2 eV [55,56]. Taking this into account, one can suggest that the high-energy emission band at 3.1 eV comes from the near-bandgap transitions. The shift of the high-energy PL band by around 0.1 eV to lower photon energy in the sample prepared via etching in the HVPE system is indicative of the presence of the rutile phase in the sample, since it is known that the bandgap of the rutile phase is around 0.1 eV lower than that inherent to the anatase phase. This observation is consistent with the results of the XRD analysis presented in Figure 3b and the Raman scattering presented in Figure 5b. The second violet PL band at 2.9 eV could be attributed to a defect, which is not identified. The green band has previously been attributed to the recombination of self-trapped excitons (STEs) made out from carrier polarons [57]. It has been suggested that, on the one hand, oxygen vacancies allow for the efficient trapping of carriers or polarons, and, on the other hand, a very efficient charge separation allows for the collection of electrons and holes or their trapping at different locations, which could be on the surface. Taking into consideration the huge surfaces of aeromaterials, one can suggest that their surfaces may play an important role in their photoluminescence processes. Note that the thickness of the microtube walls in the investigated samples is around 50 nm.

The sample annealed at 800 °C with subsequent wet etching is composed of Zn_2TiO_4 microtubes. Regarding the bandgap of Zn_2TiO_4, there is no consensus in the literature, with the reported values ranging from 3.1 eV [58] to 3.7 eV [59,60]. It could be that the high-energy PL band at 3.2 eV observed in aero-Zn_2TiO_4 is also related to near-bandgap transitions. Concerning the green PL band, its intensity in aero-Zn_2TiO_4 is even higher than

that in aero-titania. One may suggest that the internal surface and the oxygen vacancies also play an important role in the PL processes in this material.

It has previously been shown that, during the photocatalytic oxidation reaction process, oxygen vacancy defects in the nanocomposite ZnO-TiO_2 materials can act as active centers to capture photoinduced electrons, resulting in a great improvement in photocatalytic activity [30]. Oxygen vacancies also promote the adsorption on the sample of the oxygen from the environment, which results in a strong interaction between the photoexcited electron captured by oxygen vacancies and its adsorbed oxygen. Figure 8 demonstrates that the intensity of the green PL band in the prepared aeromaterials strongly decreases when an air atmosphere is introduced instead of a vacuum one. This observation can be explained by oxygen adsorption, promoted by oxygen vacancies, on the huge surfaces of aero-nanomaterials. Apart from that, the possibility to prepare various nanocomposites in a controlled manner provides opportunities for bandgap engineering and the alignment of the conduction and valence bands of the nanocomposite components with respect to the HOMO and LUMO molecular orbitals of organic compounds subjected to photocatalytic degradation. In these conditions, the photogenerated electrons move from the conduction band of one component to that of another component, while the photogenerated holes move from one valence band to another one. The excited electrons also move from the organic compounds to the conduction bands of the nanocomposite components, therefore producing reactive species for chemical reactions [33]. Taking into account the large specific surface area of the produced aeromaterials, one can also expect that surface states play an important role in shifting the edge of the valence band, therefore improving the visible light photocatalytic properties, including those related to water splitting, as shown in a first-principle study [38]. Additionally, the hetero-interfaces between nanocomposite components play an important role in improving gas-sensing properties [35].

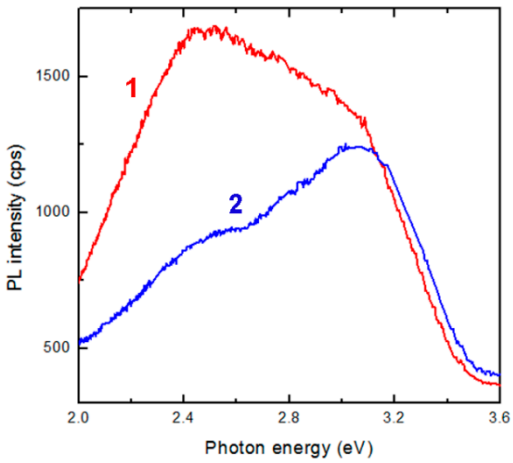

Figure 8. PL spectra of a sample annealed at 800 °C with subsequent etching in citric acid solution measured at room temperature in vacuum (curve 1) and in air (curve 2).

4. Conclusions

The results of this study demonstrate the possibility to prepare titania-based aeromaterials with a controlled morphology, composition, and crystal phase structure on the basis of ZnO-nanostructured sacrificial templates. The initial interconnected ZnO microtetrapods with cylindrical microrod legs are transformed into microtubes with various compositions upon atomic layer deposition of thin TiO_2 layers followed by the etching of the sacrificial template. The thin walls of the microtubes are dense and solid if wet etching is performed for the removal of the sacrificial template, while they are perforated if etching is performed in an HVPE system with HCl and H_2 reaction chemicals. The composition and crystal phase structure of the produced aero-nanomaterials are determined by the annealing temperature, as well as by the sequence of the technological steps. Anatase TiO_2 microtubes

are produced with annealing at 400 °C either with annealing performed before wet etching or vice versa. In the case of annealing at 800 °C, a mixture of anatase and rutile phases is obtained if wet etching is performed in the first technological step and annealing in the second one. At the same time, a spinel Zn_2TiO_4 phase is obtained with the reversal of the technological steps. Etching in an HVPE system results in the formation of a mixture of anatase and rutile phases.

The photoluminescence of the produced aero-nanomaterials is composed of three emission bands at 2.5–2.6 eV, 2.9–3.0 eV, and 3.1–3.2 eV. The high-energy PL band is supposed to be related to near-band edge emission, while the low-energy band is associated with oxygen vacancies. Taking into account that, according to previous reports, oxygen vacancies play an important role in photocatalytic properties, one may expect that the developed titania-based aero-nanomaterials are potential candidates for photocatalytic applications, as well as for sensoric applications, as demonstrated for other aeromaterials.

Supplementary Materials: The following supporting information can be downloaded at: https://www.mdpi.com/article/10.3390/cryst12121753/s1, Figure S1: SEM image of ZnO microtetrapods covered by a thin TiO_2 layer; Figure S2: Results of EDX analysis of ZnO microtetrapods covered by a thin TiO_2 layer; Figure S3: Results of EDX analysis of a sample prepared via etching in the HVPE system; Figure S4: PL spectra of a sample prepared via etching in the HVPE system measured at 10 K (curve 1) and at room temperature (curve 2); Figure S5: (**a**) Deconvolution of PL spectrum measured at 10 K and (**b**) at room temperature for a sample prepared via etching in the HVPE system.

Author Contributions: Conceptualization, V.V.U. and T.B.; methodology, V.C., S.L., V.V.Z., and S.R.; validation, P.C. and K.N.; investigation, V.C., V.V.Z., and S.L.; writing—original draft preparation, V.V.U.; writing—review and editing, V.V.U. and I.M.T.; visualization, T.B. and E.V.M.; supervision, P.C. and K.N.; project administration, I.M.T. and E.V.M.; funding acquisition, I.M.T. All authors have read and agreed to the published version of the manuscript.

Funding: This research was funded by the National Agency for Research and Development of Moldova under the Grants #20.80009.5007.20 and by the European Commission under the H2020 grant #810652 "NanoMedTwin".

Institutional Review Board Statement: Not applicable.

Informed Consent Statement: Not applicable.

Data Availability Statement: The data presented in this study are available on request from the corresponding authors.

Acknowledgments: The authors acknowledge the research team from the Christian-Albrechts University of Kiel in Germany (R. Adelung) for providing the as-grown ZnO microtetrapods.

Conflicts of Interest: The authors declare no conflict of interest. The founding sponsors had no role in the design of the study; in the collection, analyses, or interpretation of data; in the writing of the manuscript; and in the decision to publish the results.

References

1. Zhu, C.; Han, T.Y.-J.; Duoss, E.B.; Golobic, A.M.; Kuntz, J.D.; Spadaccini, C.M.; Worsley, M.A. Highly compressible 3D periodic graphene aerogel microlattices. *Nat. Commun.* **2015**, *6*, 6962. [CrossRef] [PubMed]
2. Moriche, R.; Prolongo, S.G.; Sanchez, M.; Jimenez-Suarez, A.; Campo, M.; Urena, A. Strain sensing based on multiscale composite materials reinforced with graphene nanoplatelets. *JoVE* **2016**, *117*, 54512. [CrossRef] [PubMed]
3. Shi, J.; Hu, J.; Dai, Z.; Zhao, W.; Liu, P.; Zhao, L.; Guo, Y.; Yang, T.; Zou, L.; Jiang, K.; et al. Graphene welded carbon nanotube crossbars for biaxial strain sensors. *Carbon* **2017**, *123*, 786–793. [CrossRef]
4. Cha, C.; Shin, S.R.; Annabi, N.; Dokmeci, M.R.; Khademhosseini, A. Carbon-based nanomaterials: Multi-functional materials for biomedical engineering. *ACS Nano* **2013**, *7*, 2891–2897. [CrossRef]
5. Sun, H.; Xu, Z.; Gao, C. Multifunctional, Ultra-Flyweight, Synergistically Assembled Carbon Aerogels. *Adv. Mater.* **2013**, *25*, 2554–2560. [CrossRef]
6. Mecklenburg, M.; Schuchardt, A.; Mishra, Y.K.; Kaps, S.; Adelung, R.; Lotnyk, A.; Kienle, L.; Schulte, K. Aerographite: Ultra Lightweight, Flexible Nanowall, Carbon Microtube Material with Outstanding Mechanical Performance. *Adv. Mater.* **2012**, *24*, 3486–3490. [CrossRef]

7. Tiginyanu, I.; Ghimpu, L.; Grottrup, J.; Postolache, V.; Mecklenburg, M.; Stevens-Kalceff, M.A.; Ursaki, V.; Payami, N.; Feidenhansl, R.; Schulte, K.; et al. Strong light scattering and broadband (UV to IR) photoabsorption in stretchable 3D hybrid architectures based on Aerographite decorated by ZnO nanocrystallites. *Sci. Rep.* **2016**, *6*, 32913. [CrossRef]
8. Schuchardt, A.; Braniste, T.; Mishra, Y.K.; Deng, M.; Mecklenburg, M.; Stevens-Kalceff, M.A.; Raevschi, S.; Schulte, K.; Kienle, L.; Adelung, R.; et al. Tree-Dimensional Aerographite-GaN hybrid networks: Single step fabrication of porous and mechanically fexible materials for multifunctional applications. *Sci. Rep.* **2015**, *5*, 8839. [CrossRef]
9. Plesco, I.; Dragoman, M.; Strobel, J.; Ghimpu, L.; Schütt, F.; Dinescu, A.; Ursaki, V.; Kienle, L.; Adelung, R.; Tiginyanu, I. Flexible pressure sensor based on graphene aerogel microstructures functionalized with CdS nanocrystalline thin film. *Superlattices Microstruct.* **2018**, *117*, 418–422. [CrossRef]
10. Plesco, I.; Strobel, J.; Schütt, F.; Himcinschi, C.; Sedrine, N.B.; Monteiro, T.; Rosário-Correia, M.; Gorceac, L.; Cinic, B.; Ursaki, V.; et al. Hierarchical Aerographite 3D fexible networks hybridized by InP micro/nanostructures for strain sensor applications. *Sci. Rep.* **2018**, *8*, 13880. [CrossRef]
11. Mishra, Y.K.; Kaps, S.; Schuchardt, A.; Paulowicz, I.; Jin, X.; Gedamu, D.; Freitag, S.; Claus, M.; Wille, S.; Kovalev, A.; et al. Fabrication of Macroscopically Flexible and Highly Porous 3D Semiconductor Networks from Interpenetrating Nanostructures by a Simple Flame Transport Approach. *Part. Part. Syst. Charact.* **2013**, *30*, 775–783. [CrossRef]
12. Marx, J.; Smazna, D.; Adelung, R.; Schulte, K.; Fiedler, B. Processing, growth and thermodynamic calculations of carbon foam with a hollow tetrapodal morphology-Aerographite. *Appl. Surf. Sci.* **2018**, *30*, 535–542. [CrossRef]
13. Tiginyanu, I.; Braniste, T.; Smazna, D.; Deng, M.; Schütt, F.; Schuchardt, A.; Stevens-Kalceff, M.A.; Raevschi, S.; Schürmann, U.; Kienle, L.; et al. Self-organized and self-propelled aero-GaN with dual hydrophilic/hydrophobic behavior. *Nano Energy* **2019**, *56*, 759–769. [CrossRef]
14. Plesco, I.; Braniste, T.; Wolff, N.; Gorceac, L.; Duppel, V.; Cinic, B.; Mishra, Y.K.; Sarua, A.; Adelung, R.; Kienle, L.; et al. Aero-ZnS architectures with dual hydrophilic—Hydrophobic properties for microfluidic applications. *APL Mater.* **2020**, *8*, 061105. [CrossRef]
15. Wolff, N.; Ciobanu, V.; Enachi, M.; Kamp, M.; Braniste, T.; Duppel, V.; Shree, S.; Raevschi, S.; Medina-Sánchez, M.; Adelung, R.; et al. Advanced Hybrid GaN/ZnO Nanoarchitectured Microtubes for Fluorescent Micromotors Driven by UV Light. *Small* **2020**, *16*, 1905141. [CrossRef]
16. Dragoman, M.; Braniste, T.; Iordanescu, S.; Aldrigo, M.; Raevschi, S.; Shree, S.; Adelung, R.; Tiginyanu, I. Electromagnetic interference shielding in X-band with aero-GaN. *Nanotechnology* **2019**, *30*, 34LT01. [CrossRef]
17. Braniste, T.; Zhukov, S.; Dragoman, M.; Alyabyeva, L.; Ciobanu, V.; Dragoman, D.; Iordanescu, S.; Shree, S.; Raevschi, S. Terahertz shielding properties of aero-GaN. *Semicond. Sci. Technol.* **2019**, *34*, 12LT02. [CrossRef]
18. Dragoman, M.; Ciobanu, V.; Shree, S.; Dragoman, D.; Braniste, T.; Raevschi, S.; Dinescu, A.; Sarua, A.; Mishra, Y.K.; Pugno, N.; et al. Sensing up to 40 atm Using Pressure-Sensitive Aero-GaN. *Phys. Status Solidi RRL* **2019**, *13*, 1900012. [CrossRef]
19. Braniste, T.; Dragoman, M.; Zhukov, S.; Aldrigo, M.; Ciobanu, V.; Iordanescu, S.; Alyabyeva, L.; Fumagalli, F.; Ceccone, G.; Raevschi, S.; et al. Aero-Ga_2O_3 Nanomaterial Electromagnetically Transpnarent from Microwaves to Terahertz for Internet of Things Applications. *Nanomaterials* **2020**, *10*, 1047. [CrossRef]
20. Plesco, I.; Ciobanu, V.; Braniste, T.; Ursaki, V.; Rasch, F.; Sarua, A.; Raevschi, S.; Adelung, R.; Dutta, J.; Tiginyanu, I. Highly Porous and Ultra-Lightweight Aero-Ga_2O_3: Enhancement of Photocatalytic Activity by Noble Metals. *Materials* **2021**, *14*, 1985. [CrossRef]
21. Crap, O.; Huisman, C.L.; Reller, A. Photoinduced reactivity of TiO_2. *Solid State Chem.* **2004**, *32*, 133–177.
22. Ijadpanah-Saravi, H.; Safari, M.; Khodadadi-Darban, A.; Rezaei, A. Synthesis of Titanium Dioxide Nanoparticles for Photocatalytic Degradation of Cyanide in Wastewater. *Anal. Lett.* **2014**, *47*, 1772–1782. [CrossRef]
23. Wang, J.; Yu, J.; Kong, X.Z. Preparation of hollow TiO_2 nanoparticles through TiO_2 deposition on polystyrene latex particles and characterizations of their structure and photocatalytic activity. *Nanoscale Res. Lett.* **2012**, *7*, 646. [CrossRef] [PubMed]
24. Lee, K.M.; Hu, C.W.; Chen, H.W.; Ho, K.C. Incorporating carbon nanotube in a low- temperature fabrication process for dye-sensitized TiO_2 solar cells. *Sol. Energy Mater. Sol. Cells* **2008**, *92*, 1628–1633. [CrossRef]
25. Mohammadi, M.R.; Fary, D.J.; Cordero-Cabrera, M.C. Sensor performance of nanostructured TiO_2 thin films derived from particulate sol-gel route and polymeric fugitive agents. *Sens. Actuators B-Chem.* **2007**, *124*, 74–83. [CrossRef]
26. Wang, Y.Q.; Zhang, H.M.; Wang, R.H. Investigation of the interaction between colloidal TiO_2 and bovine hemoglobin using spectral method. *Colloids Surf. B Biointerfaces* **2008**, *65*, 190–196. [CrossRef] [PubMed]
27. Haghi, M.M.; Hekmatafshar, M.B.; Janipour, S.S.; Gholizadeh, S.S.; Kazem, M.; Sayyadifar, F.; Ghaedi, M. Antibacterial effect of TiO_2 nanoparticles on pathogenic strain of *E. coli*. *Int. J. Adv. Biotechnol. Res.* **2012**, *3*, 621–624.
28. Zhang, Q.; Fan, W.; Gao, L. Anatase TiO_2 nanoparticles immobilized on ZnO tetrapods as a highly efficient and easily recyclable photocatalyst. *Appl. Catal. B Environ.* **2007**, *76*, 168–173. [CrossRef]
29. Lopera, A.A.; Velasquez, A.M.; Chavarriaga, E.A.; Ocampo, S.; Zaghete, M.A.; Graminha, M.A.; Garcia, C.P. Synthesis by combustion in solution of Zn_2TiO_4+Ag for photocatalytic and photodynamic applications in the visible. *J. Phys. Conf. Ser.* **2017**, *935*, 012013. [CrossRef]
30. Qin, X.; Cui, L.; Shao, G. Preparation of ZnO-Zn_2TiO_4. Sol Composite Films and Its Photocatalytic Activities. *J. Nanomater.* **2013**, *2013*, 428419. [CrossRef]
31. Khatua, L.; Sahoo, R.; Satapathy, P.; Panda, R.; Das, S.K. Visible light photocatalytic dye decomposition behaviour of solid state reaction grown Zn_2TiO_4 nanoparticles. *J. Semicond.* **2018**, *39*, 123002. [CrossRef]

32. Khatua, L.; Panda, R.; Nayak, R.; Singh, A.; Sahoo, P.K.; Pradhan, D.; Singh, U.D.; Das, S.K. Efficient UV photocatalytic dye decomposition activity with cost effective solid state reaction grown Zinc Orthotitanate (Zn_2TiO_4) nanoparticles. *J. Alloys Comp.* **2018**, *764*, 895–900. [CrossRef]
33. Mahajan, J.; Jeevanandam, P. Synthesis of Zn_2TiO_4@CdS Core-shell Heteronanostructures by Novel Thermal Decomposition Approach for Photocatalytic Application. *Chem. Sel.* **2019**, *4*, 12580–12591.
34. Gaidan, I.; Brabazon, D.; Ahad, I.U. Response of a Zn_2TiO_4 Gas Sensor to Propanol at Room Temperature. *Sensors* **2017**, *17*, 1995. [CrossRef]
35. Chen, X.-Y.; Wang, X.-Z.; Liu, F.-J.; Zhang, G.-S.; Song, X.-J.; Cui, H.-Z. Fabrication of porous Zn_2TiO_4—ZnO microtubes and analysis of their acetone gas sensing properties. *Rare Met.* **2021**, *40*, 1528–1535. [CrossRef]
36. Wana, L.; Li, X.; Qu, Z.; Shi, Y.; Li, H.; Zhao, Q.; Chen, G. Facile synthesis of ZnO/Zn_2TiO_4 core/shell nanowires for photocatalytic oxidation of acetone. *J. Hazard. Mater.* **2010**, *184*, 864–868. [CrossRef]
37. Sun, X.; Wang, S.; Shen, C.; Xu, X. Efficient Photocatalytic Hydrogen Production over Rh-Doped Inverse Spinel Zn_2TiO_4. *ChemCatChem* **2016**, *8*, 2289–2295. [CrossRef]
38. Fu, Q.; Guo, L. Band-engineered Zn_2TiO_4 nanowires for hydrogen generation from water using visible light: A first-principles study. *AIP Adv.* **2022**, *12*, 015201. [CrossRef]
39. Mrazek, J.; Spanhel, L.; Surynek, M.; Potel, M.; Matejec, V. Crystallization properties of RE-doped (RE = Eu, Er, Tm) Zn_2TiO_4 prepared by the sol-gel method. *J. Alloy. Comp.* **2011**, *509*, 4018–4024. [CrossRef]
40. Li, J.; Wu, B.; Zhang, Q.; Wang, H.; Li, Y. Highly Luminescent Mesoporous Zn_2TiO_4:Eu^{3+} Material with Excellent Sensing and Removal Abilities for Heavy-Metal Ions. *J. Nanosci. Nanotechnol.* **2016**, *16*, 9568–9574. [CrossRef]
41. Girish, K.M.; Naik, R.; Prashantha, S.C.; Nagabhushana, H.; Nagaswarupa, H.P.; Raju, K.S.A.; Premkumar, H.B.; Sharma, S.C.; Nagabhushana, B.M. Zn_2TiO_4:Eu^{3+} nanophosphor: Self explosive route and its near UV excited photoluminescence properties for WLEDs. *Spectrochim. Acta Part A Mol. Biomol. Spectrosc.* **2015**, *138*, 857–865. [CrossRef] [PubMed]
42. Austin, A.J.; Echeverria, E.; Wagle, P.; Mainali, P.; Meyers, D.; Gupta, A.K.; Sachan, R.; Prassana, S.; McIlroy, D.N. High Temperature Atomic Layer Deposition of GaN on 1D Nanostructures. *Nanomaterials* **2020**, *10*, 2434. [CrossRef] [PubMed]
43. Bachmann, J. (Ed.) *Atomic Layer Deposition in Energy Conversion Applications*; Wiley-VCH Verlag GmbH & Co KGaA: Weinheim, Germany, 2017; p. 312.
44. Sridharan, K.; Jang, E.; Park, Y.M.; Park, T.G. Superior Photostability and Photocatalytic Activity of ZnO Nanoparticles Coated with Ultrathin TiO_2 Layers through AtomicLayer Deposition. *Chem. Eur. J.* **2015**, *21*, 19136–19141. [CrossRef] [PubMed]
45. Katoch, A.; Kim, J.-H.; Kim, S.S. TiO_2/ZnO Inner/Outer Double-Layer Hollow Fibers for Improved Detection of Reducing Gases. *ACS Appl. Mater. Interfaces* **2014**, *6*, 21494–21499. [CrossRef] [PubMed]
46. Ku, C.-S.; Lee, H.-Y.; Huang, J.-M.; Lin, C.-M. Epitaxial growth of ZnO films at extremely low temperature by atomic layer deposition with interrupted flow. *Mater. Chem. Phys.* **2010**, *120*, 236–239. [CrossRef]
47. Yang, J.; Bahrami, A.; Ding, X.; Lehmann, S.; Kruse, N.; He, S.; Wang, B.; Hantusch, M.; Nielsch, K. Characteristics of ALD-ZnO Thin Film Transistor Using H_2O and H_2O_2 as Oxygen Sources. *Adv. Mater. Int.* **2022**, *9*, 2101953. [CrossRef]
48. He, S.; Bahrami, A.; Zhang, X.; Martinez, I.G.; Lehmann, S.; Nielsh, K. Effect of Powder ALD Interface Modification on the Thermoelectric Performance of Bismuth. *Adv. Mater. Technol.* **2022**, *7*, 2100953. [CrossRef]
49. Zak, A.K.; Razali, R.; Abd Majid, W.H.; Darroudi, M. Synthesis and characterization of a narrow size distribution of zinc oxide nanoparticles. *Int. J. Nanomed.* **2011**, *6*, 1399–1403.
50. Arin, J.; Thongtem, S.; Phuruangrat, A.; Thongtem, T. Characterization of ZnO-TiO_2 and zinc titanate nanoparticles synthesized by hydrothermal process. *Res. Chem. Intermed.* **2017**, *43*, 3183–3195. [CrossRef]
51. Ohsaka, T.; Izumi, F.; Fujiki, Y. Raman spectrum of anatase TiO_2. *J. Raman Spectrosc.* **1978**, *7*, 321–324. [CrossRef]
52. Porto, S.P.S.; Fleuri, P.A.; Damen, T.C. Raman Syectra of TiO_2, MgF, ZnF, FeFs, and MnF. *Phys. Rev.* **1967**, *154*, 522–524. [CrossRef]
53. Frank, O.; Zukalova, M.; Laskova, B.; Kurti, J.; Koltai, J.; Kavan, L. Raman spectra of titanium dioxide (anatase, rutile) with identified oxygen isotopes (16, 17, 18). *Phys. Chem. Chem. Phys.* **2012**, *14*, 14567–14572. [CrossRef] [PubMed]
54. Li, L.; Gao, S.; Cui, T.; Li, B.; Zhou, Q.; Yuan, H.; Xu, D. Temperature-dependent optical phonon behaviour of a spinel Zn_2TiO_4 single crystal grown by the optical floating zone method in argon atmosphere. *RSC Adv.* **2017**, *7*, 35477. [CrossRef]
55. Dette, C.; Perez-Osorie, M.A.; Kley, C.S.; Punke, P.; Patrick, C.E.; Jacobson, P.; Giustino, F.; Jung, S.J.; Kern, K. TiO_2 anatase with a bandgap in the visible region. *Nano Lett.* **2014**, *14*, 6533–6538. [CrossRef]
56. Reddy, K.M.; Manorama, S.V.; Reddy, A.R. Bandgap studies on anatase titanium dioxide nanoparticles. *Mater. Chem. Phys.* **2002**, *78*, 239–245. [CrossRef]
57. Gallart, M.; Cottineau, T.; Honerlage, B.; Keller, N.; Keller, V.; Gilliot, P. Temperature dependent photoluminescence of anatase and rutile TiO_2 single crystals: Polaron and self-trapped exciton formation. *J. Appl. Phys.* **2018**, *124*, 133104. [CrossRef]
58. Ali, Z.; Ali, S.; Ahmad, S.I.; Khan, I.; Aliabad, H.A.R. Structural and optoelectronic properties of the zinc titanate perovskite and spinel by modified Becke-Johnson potential. *Phys. B* **2013**, *420*, 54–57. [CrossRef]
59. Song, J.; Leng, M.; Xiao, H.; Zhang, L.; Qin, Y.; Hou, W.; Du, N.; Liu, J. Preparation of Single Phase Zn_2TiO_4 Spinel from a New ZnTi Layered Double Hydroxide Precursor. *J. Nanosci. Nanotechnol.* **2014**, *14*, 4649–4654. [CrossRef] [PubMed]
60. Mayen-Hernandez, S.A.; Torres-Delgado, G.; Castanedo-Perez, R.; Villarreal, M.G.; Cruz-Orea, A.; Alvarez, J.G.M.; Zelaya-Angel, O. Optical and structural properties of ZnO + Zn_2TiO_4 thin films prepared by the sol-gel method. *J. Mater. Sci. Mater. Electron.* **2007**, *18*, 1127–1130. [CrossRef]